Article

Plasticity in single-crystalline Mg_3Bi_2 thermoelectric material

https://doi.org/10.1038/s41586-024-07621-8

Received: 29 September 2023

Accepted: 29 May 2024

Published online: 10 July 2024

Check for updates

Peng Zhao[1,9], Wenhua Xue[1,2,9], Yue Zhang[2,9], Shizhen Zhi[1], Xiaojing Ma[1], Jiamin Qiu[1], Tianyu Zhang[1], Sheng Ye[1], Huimin Mu[3], Jinxuan Cheng[1], Xiaodong Wang[1,4], Shuaihang Hou[1], Lijia Zhao[5], Guoqiang Xie[1,6], Feng Cao[7], Xingjun Liu[1,6], Jun Mao[1,6]✉, Yuhao Fu[3]✉, Yumei Wang[2,8]✉ & Qian Zhang[1,6]✉

Most of the state-of-the-art thermoelectric materials are inorganic semiconductors. Owing to the directional covalent bonding, they usually show limited plasticity at room temperature[1,2], for example, with a tensile strain of less than five per cent. Here we discover that single-crystalline Mg_3Bi_2 shows a room-temperature tensile strain of up to 100 per cent when the tension is applied along the (0001) plane (that is, the *ab* plane). Such a value is at least one order of magnitude higher than that of traditional thermoelectric materials and outperforms many metals that crystallize in a similar structure. Experimentally, slip bands and dislocations are identified in the deformed Mg_3Bi_2, indicating the gliding of dislocations as the microscopic mechanism of plastic deformation. Analysis of chemical bonding reveals multiple planes with low slipping barrier energy, suggesting the existence of several slip systems in Mg_3Bi_2. In addition, continuous dynamic bonding during the slipping process prevents the cleavage of the atomic plane, thus sustaining a large plastic deformation. Importantly, the tellurium-doped single-crystalline Mg_3Bi_2 shows a power factor of about 55 microwatts per centimetre per kelvin squared and a figure of merit of about 0.65 at room temperature along the *ab* plane, which outperforms the existing ductile thermoelectric materials[3,4].

Metals are usually malleable and ductile, benefitting from the metallic bonding that involves a strong electrostatic force between the delocalized electrons and metal cations. In contrast, semiconductors are brittle owing to the directional covalent or ionic bonding, and repulsive interaction appears when atoms slide[5]. Traditional thermoelectric materials are inorganic semiconductors and they show limited deformability.

Recently, some inorganic semiconductors with plastic deformability have been reported, for example, Ag_2S alloys[3,4,6], ZnS (ref. 7), InSe (ref. 8) and several van der Waals materials[9]. As flexible thermoelectric devices mainly aim at applications such as human body heat harvesting and personalized thermoregulation[3,10], materials with high thermoelectric performance at ambient temperature are highly desirable. Unfortunately, room-temperature thermoelectric materials are limited[11], let alone the additional requirement for plastic deformability. Here we discover that Mg_3Bi_2 single crystals are plastic at room temperature, and they also show promising thermoelectric properties that outperform the state-of-the-art ductile semiconductors.

Plasticity in Mg_3Bi_2 single crystal

Mg_3Bi_2 crystallizes in the typical anti-α-La_2O_3 structure type ($P\bar{3}m1$), as shown in Fig. 1a. To characterize the plastic deformability of Mg_3Bi_2-based materials, both single-crystalline (S) and polycrystalline (P) samples were prepared (Supplementary Figs. 1–6). Both polycrystalline and single-crystalline Mg_3Bi_2 can realize large compressive strains above 50% (Fig. 1b,h). In comparison, thermoelectric materials such as $Bi_{0.5}Sb_{1.5}Te_3$, $Bi_2Te_{2.7}Se_{0.3}$, GeTe and ZrNiSn show a maximum compressive strain of less than 5% (Fig. 1b and Supplementary Fig. 7). As Mg_3Bi_2 crystallizes in the hexagonal lattice (Fig. 1a), a comparison of the tensile stress–strain curves between Mg_3Bi_2 and several hexagonal close-packed (hcp) metals along with other ductile semiconductors has been made (Fig. 1c and Supplementary Fig. 8). The single-crystalline Mg_3Bi_2 withstands a tensile strain of up to 100%, which is higher than that of hcp metals and ductile semiconductors and comparable to annealed $Ag_2Te_{0.7}S_{0.3}$ (ref. 4).

As shown in Fig. 1d, the tensile properties of the single-crystalline Mg_3Bi_2 are highly anisotropic. When the tension is applied along (0001) plane (that is, $\theta = 0°$), it can realize a large tensile strain of about 100%. However, when the tension is applied along the direction with a non-zero angle (that is, $\theta \neq 0°$) with respect to the (0001) plane (Fig. 1d, inset), the maximum tensile strain reduces markedly, and it is only about 12% when the angle is about 40°. Such anisotropy should be attributed to the easy cleavage between the *ab* plane. When tension is applied along the direction with a non-zero angle

[1]School of Materials Science and Engineering, and Institute of Materials Genome and Big Data, Harbin Institute of Technology (Shenzhen), Shenzhen, People's Republic of China. [2]Beijing National Laboratory for Condensed Matter Physics, Institute of Physics, Chinese Academy of Sciences, Beijing, People's Republic of China. [3]State Key Laboratory of Superhard Materials, Key Laboratory of Material Simulation Methods and Software of Ministry of Education, College of Physics, Jilin University, Changchun, People's Republic of China. [4]Institute of Special Environments Physical Sciences, Harbin Institute of Technology (Shenzhen), Shenzhen, People's Republic of China. [5]Key Laboratory of Electromagnetic Processing of Materials (Ministry of Education), Northeastern University, Shenyang, People's Republic of China. [6]State Key Laboratory of Advanced Welding and Joining, Harbin Institute of Technology, Harbin, People's Republic of China. [7]School of Science, Harbin Institute of Technology (Shenzhen), Shenzhen, People's Republic of China. [8]Beijing Branch of Songshan Lake Materials Laboratory, Dongguan, People's Republic of China. [9]These authors contributed equally: Peng Zhao, Wenhua Xue, Yue Zhang. ✉e-mail: maojun@hit.edu.cn; yuhao_fu@jlu.edu.cn; wangym@iphy.ac.cn; zhangqf@hit.edu.cn

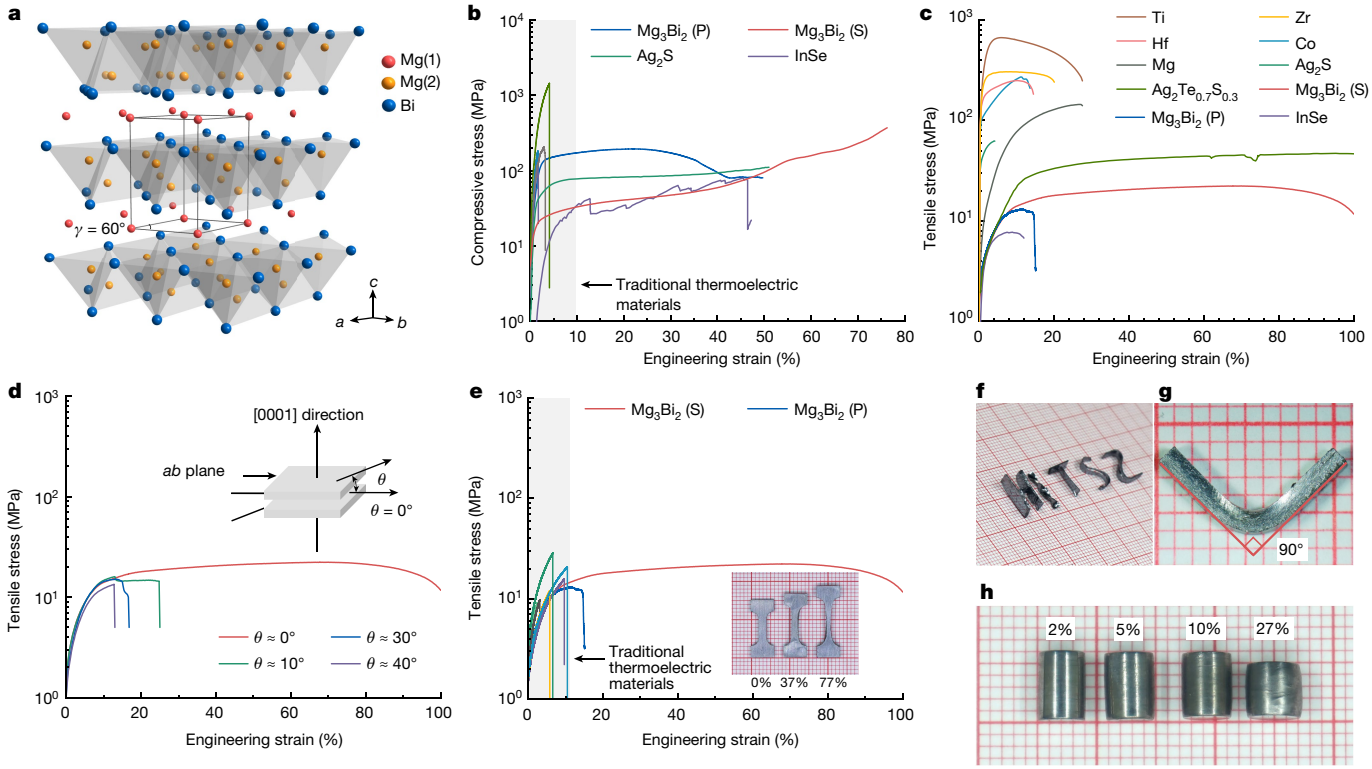

Fig. 1 | Plastic deformability of Mg_3Bi_2. a, The crystal structure of Mg_3Bi_2, where γ is the supplementary angle between the a and b axes. **b**, Compressive stress–strain curves of different thermoelectric materials and ductile semiconductors. **c**, Tensile stress–strain curves of different hcp metals and ductile semiconductors. The data for Ti, Zr, Mg, Hf and Co were obtained in this work. **d**, Anisotropic tensile properties of single-crystalline Mg_3Bi_2. Inset: the schematic view shows the angle (θ) between the tension and the ab plane. **e**, Tensile stress–strain curves of different thermoelectric materials. Inset: comparison between the elongated and the pristine single-crystalline Mg_3Bi_2. The data for $Bi_{0.5}Sb_{1.5}Te_3$, $Bi_2Te_{2.7}Se_{0.3}$, GeTe-based, PbTe-based, MgAgSb and ZrCoSb were obtained in this work. **f**, Morphed single-crystalline Mg_3Bi_2 showing the letters 'HITSZ'. **g**, Bent single-crystalline Mg_3Bi_2. **h**, Comparison of the bulk polycrystalline Mg_3Bi_2 with different compressive deformation.

with respect to the (0001) plane, a component of the tension along [0001] direction will result in the cleavage of the single-crystalline Mg_3Bi_2. This also partially explains why the maximum tensile strain of the polycrystalline sample is lower than that of the single crystal. In the following discussion, all the tensile stress–strain curves of the Mg_3Bi_2 single crystals are characterized with the tension applied along the (0001) plane.

A comparison of the tensile properties between Mg_3Bi_2 and traditional thermoelectric materials is shown in Fig. 1e and Supplementary Fig. 9. The maximum tensile strain of single-crystalline Mg_3Bi_2 is one order of magnitude higher than that of traditional thermoelectric materials. The inset of Fig. 1e shows the elongated single crystals with different tensile strains. It is noteworthy that the single-crystalline Mg_3Bi_2 can be easily deformed, and it has been folded, twisted or bent into the letters showing 'HITSZ' (Fig. 1f). In addition, the three-point bending test has also been conducted on the single-crystalline Mg_3Bi_2. The two ends of the bent sample are barely affected and maintain a 90° angle (Fig. 1g and Supplementary Fig. 10), indicating a localized plastic deformation. The deformability not only exists in single crystals but also is noticeable in polycrystalline Mg_3Bi_2. The bulk cylinder of the polycrystalline sample can be easily compressed (Fig. 1h) and machined into the long lathes (Supplementary Fig. 11).

The microscopic mechanism for plasticity

To understand the microscopic mechanism of the plastic deformation in Mg_3Bi_2, microstructural characterizations were performed. Slip bands in the deformed Mg_3Bi_2 were identified (Fig. 2a and Supplementary Fig. 12), indicating the collective gliding of high-density dislocations (Supplementary Fig. 13). To further characterize the dislocations and identify the slip systems, high-angle annular dark-field scanning transmission electron microscopy (HAADF-STEM) was applied (Fig. 2 and Supplementary Figs. 14 and 15). Figure 2b–i and Supplementary Fig. 15 show the edge dislocations in the deformed Mg_3Bi_2 single crystal. The Burgers vector of the neighbouring edge dislocations is in the direction of $[11\bar{2}\bar{1}.\bar{2}]$ and its magnitude is $2d_{(11\bar{2}\bar{2})}$, where $d_{(11\bar{2}\bar{2})}$ is the spacing between the neighbouring $(11\bar{2}\bar{2})$ planes. Extra half-planes $(10\bar{1}\bar{1})$ and $(01\bar{1}\bar{1})$ and the slip plane $(1\bar{1}00)$ can be determined from the STEM images in Fig. 2b and Supplementary Fig. 15d. To distinctly show the dislocation core, a filtering processing was preformed for Fig. 2c. The obtained filtered images from diffraction spots $10\bar{1}\bar{1}$ and $01\bar{1}\bar{1}$ clearly show the inserted extra half-plane in Fig. 2d,e, respectively. As Mg_3Bi_2 crystallizes in a hexagonal lattice, it is reasonable to expect the slip systems in Mg_3Bi_2 to be similar to those in the hcp metals[12]. The main slip systems in the hcp metals include the basal slip $\{0001\}\langle 11\bar{2}0\rangle$, the prismatic slip $\{1\bar{1}00\}\langle 11\bar{2}0\rangle$ and $\{1\bar{1}00\}\langle 11\bar{2}\bar{3}\rangle$, and the pyramidal slip $\{1\bar{1}01\}\langle 11\bar{2}0\rangle$, $\{1\bar{1}01\}\langle \bar{1}2\bar{1}3\rangle$ and $\{11\bar{2}\bar{2}\}\langle \bar{1}\bar{1}23\rangle$ (Supplementary Fig. 16)[13–15]. Experimentally, the observed Burgers vector can be viewed as the projection of vectors of $[11\bar{2}\bar{3}]$ and/or $[11\bar{2}0]$. Therefore, the edge dislocations in the deformed Mg_3Bi_2 can be generated by the activation of the $\{1\bar{1}00\}\langle 11\bar{2}\bar{3}\rangle$ and/or $\{1\bar{1}00\}\langle 11\bar{2}0\rangle$ slip systems (Fig. 2f), that is, the prismatic $\langle c+a\rangle$ and/or $\langle a\rangle$ slip systems. As the tension is applied perpendicular to the [0001] direction, the activation of the $\{1\bar{1}00\}\langle 11\bar{2}\bar{3}\rangle$ and/or $\{1\bar{1}00\}\langle 11\bar{2}0\rangle$ slip systems can contribute to the plastic deformation in Mg_3Bi_2.

In addition, edge dislocations with Burgers vector $\boldsymbol{b} = c[0001]$ corresponding to the slip plane $(1\bar{2}10)$ (Fig. 2g) were observed. The filtered image from the diffraction spot 0002 in Fig. 2g clearly shows the

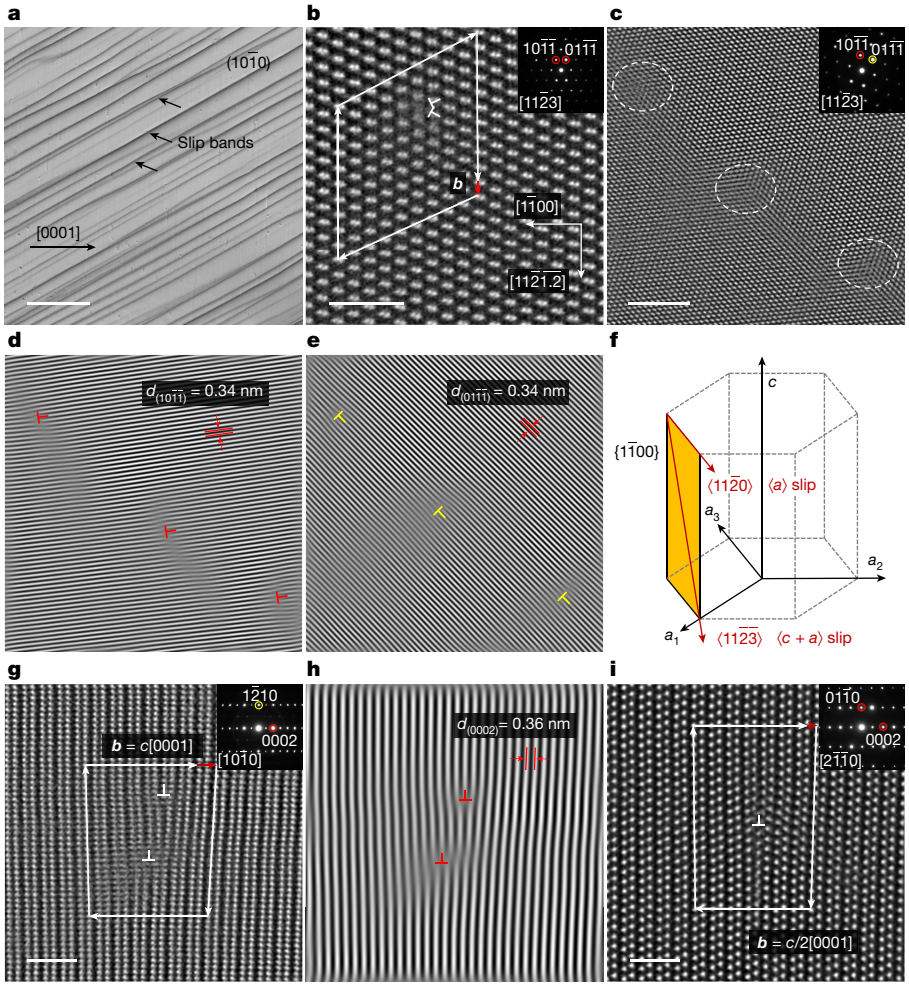

Fig. 2 | Microstructural characterization of the deformed single-crystalline Mg_3Bi_2. **a**, Scanning electron microscopy image of deformed Mg_3Bi_2 (with 10% strain) showing sharp slip bands. **b**, [11$\bar{2}$3] HAADF-STEM image showing multiple neighbouring edge dislocations with Burgers vector in the direction of [11$\bar{2}$1.$\bar{2}$] and a magnitude of $2d_{(11\bar{2}\bar{2})}$. The dislocations are marked by the white ⊥. Inset: the corresponding selected area electron diffraction (SAED) pattern with the indexed spots 10$\bar{1}$1 and 01$\bar{1}$1 marked by the red circles. **c**, the [11$\bar{2}$3] HAADF-STEM image showing multiple cores of dislocations marked by the dashed white circles. Inset: the corresponding SAED pattern with indexed spots 10$\bar{1}$1 and 01$\bar{1}$1. **d**,**e**, The obtained filtered images from the diffraction spots indicated by the red and yellow circles in the inset of **c**, respectively. The dislocations are marked by red and yellow ⊥, respectively, and the interplanar spacing of (10$\bar{1}$1) and (01$\bar{1}$1) is about 0.34 nm. **f**, Schematic view of the slip systems in Mg_3Bi_2. **g**, [10$\bar{1}$0] HAADF-STEM image showing edge dislocations with Burgers vector $\boldsymbol{b} = c$[0001]. Inset: SAED pattern with the indexed spots 1$\bar{2}$10 and 0002 marked with yellow and red circles. **h**, The filtered image of **g**. The dislocations are marked with red ⊥ and the interplanar spacing of (0002) is about 0.36 nm. **i**, [2$\bar{1}\bar{1}$0] HAADF-STEM image showing an edge dislocation with Burgers vector $\boldsymbol{b} = c/2$[0001], the dislocation is marked with the white ⊥. Inset: SAED pattern with the indexed spots 01$\bar{1}$0 and 0002 marked with red circles. The white arrows show the Burgers circuits and the red arrows are the Burgers vector in **b**,**g**,**i**. Scale bars, 20 μm (**a**), 2 nm (**b**), 5 nm (**c**), 2 nm (**g**,**i**).

inserted extra half-plane (Fig. 2h). In addition, edge dislocations with Burgers vector $\boldsymbol{b} = c/2$[0001] corresponding to the slip plane (01$\bar{1}$0) were also observed (Fig. 2i), suggesting slip of the atomic plane along the [0001] direction during plastic deformation. However, when tension is applied perpendicular to the [0001] direction, such slip along the [0001] direction should be difficult. In principle, the slip process is governed by Schmid's law, that is, the shear stress applied along the slip direction should be larger than the corresponding critically resolved shear stress. Therefore, whether a certain slip system can be activated in a single crystal depends on the relation between crystal orientation and the direction of tension. According to Schmid's law, the resolved shear stress along the [0001] direction is negligible when the tension is applied perpendicular to the [0001] direction. In the tensile test, crystal rotation occurs when plastic deformation becomes noticeable (Supplementary Fig. 17). In this scenario, non-vanishing resolved shear stress along the [0001] direction can be produced, and the slip across the (0001) planes becomes possible and contributes partly to the plastic deformability.

Density functional theory calculations were performed to further understand the slip systems in Mg_3Bi_2. Specifically, basal, prismatic and pyramidal slip systems with slip direction along ⟨11$\bar{2}$0⟩ and ⟨11$\bar{2}$3⟩ were considered (Supplementary Fig. 18 and Supplementary Tables 1 and 2). During slipping, the position of the slip planes and their interlayer distance can be changed. This process is simulated by dividing the slip within one crystallographic period along the slip directions of ⟨11$\bar{2}$0⟩ and ⟨11$\bar{2}$3⟩ into 30 steps. For every step, the total energy as a function of interlayer distance (d) is calculated. The slipping barrier energy (ΔE_s) is the change in energies between the material's initial total energy and the state with the largest energy during slipping. The large plastic deformability requires the material to have a low slipping barrier energy along the slipping plane. Figure 3a,b shows that the slipping barrier energy of the slip system {1$\bar{1}$00}⟨11$\bar{2}$3⟩ is about 39 meV Å^{-2} and it is about 20 meV Å^{-2} for the slip system {1$\bar{1}$00}⟨11$\bar{2}$0⟩ (Supplementary Fig. 19). The low slipping barrier energy of the prismatic slip systems explains the observed edge dislocations with Burgers vector in the direction of [11$\bar{2}$1.$\bar{2}$] and the magnitude of $2d_{(11\bar{2}\bar{2})}$. Compared with the slip of the whole atomic plane that involves the breaking and reforming of the chemical bonds, edge dislocation requires only the additional atomic plane to move a very short distance. Therefore, the existence of the dislocations can greatly reduce the slipping barrier energy and further facilitate the slipping process. In addition, the slipping barrier energy for all the other slip systems is less than 55 meV Å^{-2} (Supplementary Figs. 19 and 20). Similarly, Ag_2S and InSe also have low slipping barrier energies along certain crystallographic planes (Supplementary Fig. 21). Therefore, this suggests that multiple slip systems are possible in Mg_3Bi_2, which can account for the plasticity of this material. In addition to the low slipping barrier energy, the atoms between the neighbouring slipping planes should have strong interaction to prevent cleavage and the formation of cracks, that is, high cleavage energy (ΔE_c). As shown in Supplementary Table 3, the atomic planes in Mg_3Bi_2 have relatively high cleavage energy during slipping. Besides, the slipping barrier energy and cleavage energy of different 1-2-2 Zintl phase materials have been calculated (Supplementary Table 4). There are several materials with higher values for the ratio of cleavage energy to slipping barrier energy than that of Mg_3Bi_2, suggesting possible plasticity in single-crystalline samples.

To gain more insight into the microscopic mechanism for the plasticity, an analysis of the chemical bonding in Mg_3Bi_2 was performed.

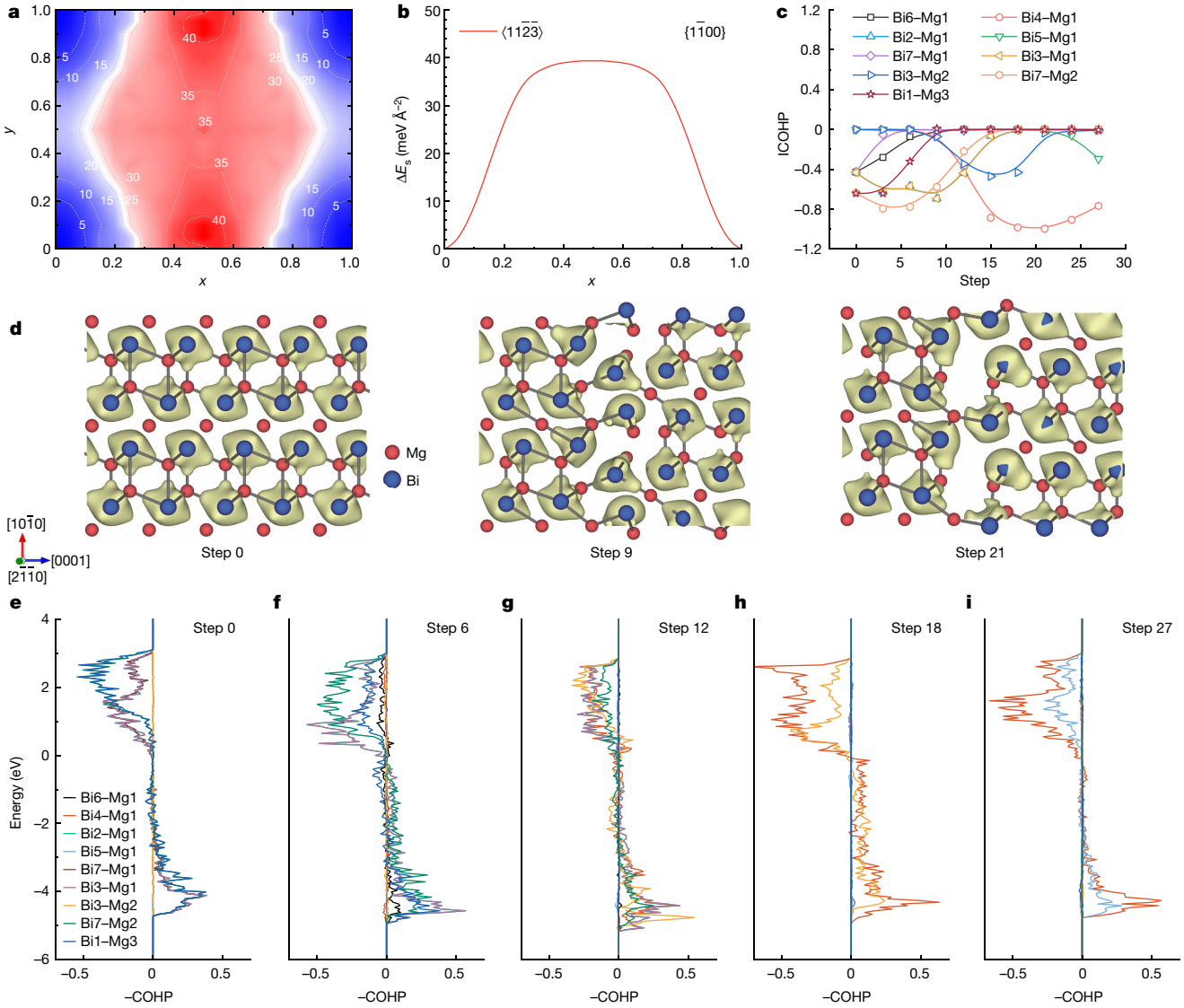

Fig. 3 | Bonding feature and slipping in Mg_3Bi_2. **a**, Contour plot for the calculated slipping barrier energy of the $(1\bar{1}00)$ plane. The unit for the values in the figure is meV Å^{-2}. **b**, Slipping barrier energy of the $\{1\bar{1}00\}$ plane along the $\langle 11\bar{2}\bar{3}\rangle$ direction. **c**, ICOHP for steps of slipping along the $\langle 11\bar{2}\bar{3}\rangle$ direction. **d**, The evolution of the electron localization function in Mg_3Bi_2 for different steps along the $\langle 11\bar{2}\bar{3}\rangle$ direction with an isosurface value of 0.7. **e**–**i**, −COHP for slipping steps 0 (**e**), 6 (**f**), 12 (**g**), 18 (**h**) and 27 (**i**) along the $\langle 11\bar{2}\bar{3}\rangle$ direction.

The electron localization function, which is the probability of finding an electron pair in a space region, is an intuitive tool that enables the visualization of bonding pairs. The calculated electron localization function for prismatic slip systems $\{1\bar{1}00\}\langle 11\bar{2}\bar{3}\rangle$ and $\{1\bar{1}00\}\langle 11\bar{2}0\rangle$ shows significant dynamic bonding near the slip plane (Fig. 3d and Supplementary Fig. 22). The integrated crystal orbital Hamilton population (ICOHP), which quantifies the bonding strength for each step of the slipping process visualizing these bonds, is also calculated as shown in Fig. 3c. Schematic diagrams of the slipping interfaces of Mg_3Bi_2 are shown in Supplementary Fig. 23 and the calculated crystal orbital Hamilton population (COHP) of other slip system is shown in Supplementary Figs. 24–26. Despite continuous breaking and reforming of magnesium (Mg)–bismuth (Bi) bonds during the slipping process, robust dynamic bonding persists at each step, thus preventing the fracture of the material, and it is quite similar to Ag_2S (refs. 6,16; Supplementary Figs. 27 and 28). During the slip process, there are multiple slip pathways in Ag_2S, and the silver (Ag)–sulfur (S) octagon framework moves easily, accompanied by the formation of Ag–Ag metallic bonds[16]. However, there are also some differences between the two materials. According to the COHP calculations, the Ag–S bonds are strongly antibonding near the valence-band edges in Ag_2S (Supplementary Fig. 29d). Conversely, the Mg–Bi bonds are mainly bonding states near valence-band edges. In particular, the bonding between Mg and Bi is relatively weak near the valence-band maximum and gradually strengthens when moving into valence bands (Supplementary Fig. 29c).

It is noted that elemental Mg shows limited plasticity due to the restricted basal slip $\{0001\}\langle 11\bar{2}0\rangle$ and tensile twin $\{10\bar{1}2\}\langle 10\bar{1}\bar{1}\rangle$ [13,15]. However, it becomes much more malleable when alloyed with other elements[17–21], owing to the additional activation of other slip systems. Similarly, Bi is a semimetal whose 6*p* orbital energy (−0.17519 eV) is almost degenerate with the 3*s* orbital energy (−0.17563 eV) of Mg when relativistic effects are considered[22]. This metallic tendency and orbital energy similarity leads to partial metallic-like bonding between Mg and Bi. Notably, the electronegativity difference between the elements (for example, Mg 1.31 and Bi 2.02) indicates more intricate bonding in Mg_3Bi_2, potentially involving ionic, covalent and metallic interactions. Mg_3Bi_2 is a typical Zintl phase structure composed of metallic Mg and metalloid Bi. According to the Zintl chemical rules, as the main group elements become heavier, their bonding shows a more metallic

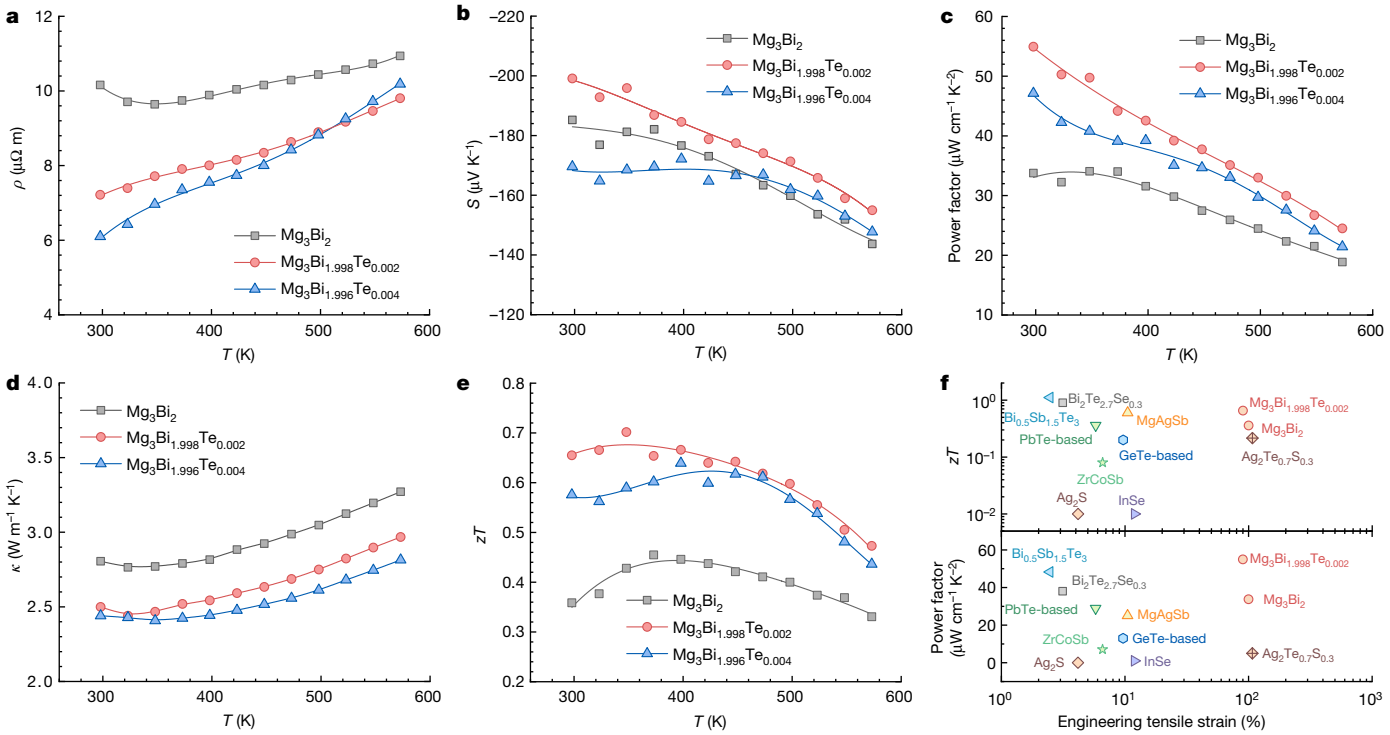

Fig. 4 | Thermoelectric properties of the single-crystalline $Mg_3Bi_{2-x}Te_x$ along the *ab* plane. a–**e**, Temperature-dependent electrical resistivity (**a**), Seebeck coefficient (**b**), power factor (**c**), thermal conductivity (**d**) and zT (**e**) of $Mg_3Bi_{2-x}Te_x$. It is noted that the thermoelectric properties of $Mg_3Bi_{2-x}Te_x$ are measured along the *ab* plane. **f**, Comparison of the relationship between the maximum engineering tensile strain and room-temperature zT and power factor among the different thermoelectric materials.

character[23]. Consequently, the mechanical properties of Mg_3Bi_2 are expected to be more metallic-like, consistent with the discussed bonding analysis and its semi-metallic nature. This mixed bonding feature, especially the presence of partial metallic bonding, has weak, non-local characteristics, which can improve the material's tolerance to atomic movement during deformation. In addition, the interlayer Mg1 bonds with multiple adjacent Bi atoms (coordination number is 6), which is also conducive to maintaining dynamic bonding. Thus, the mixed bonding of Mg_3Bi_2 shares similarities with the weak, diffuse and multicentred Ag–S bond in Ag_2S (ref. 6). This multifaceted bonding is the key to the unexpected plasticity of Mg_3Bi_2.

Thermoelectric performance of $Mg_3Bi_{2-x}Te_x$

Mg_3Bi_2-based alloys with promising thermoelectric performance around room temperature have been reported[24,25]. Our results show that the thermoelectric properties of the n-type single-crystalline Mg_3Bi_2 are highly anisotropic (Supplementary Figs. 30–32). The electrical resistivity (ρ) and the Seebeck coefficient (S) of $Mg_3Bi_{2-x}Te_x$ are higher in the *ab* plane than in the *c* plane and the thermal conductivity (κ) is higher in the *c* plane than in the *ab* plane. Such abnormal anisotropy should be ascribed to the semi-metallic nature of the Mg_3Bi_2-based materials (Supplementary Figs. 33 and 34), that is, the transport properties are jointly determined by the electrons and holes. The valence band is highly anisotropic and the hole effective mass along the Γ–A direction (along the *c* direction) is only about $0.002m_0$, whereas it is about $0.77m_0$ along the K′–Γ–K direction (in the *ab* plane) and about $0.88m_0$ along the M′–Γ–M direction (in the *ab* plane), where m_0 is the free electron mass. The much smaller hole effective mass along the Γ–A direction contributes to higher hole mobility and eventually leads to lower resistivity and larger electronic thermal conductivity in the *c* plane. Calculation of the transport properties has also been performed by the BoltzTraP2 code (Supplementary Fig. 35), and their trends are in reasonably good agreement with the measured results. The calculation also suggests reduced anisotropy at higher electron concentrations, which can be attributed to the disappearance of the isoenergy surface of the valence band (Supplementary Fig. 36). It should be noted that our results are in good agreement with a recent report[26] (Supplementary Fig. 37).

The thermoelectric properties of $Mg_3Bi_{2-x}Te_x$ along the *ab* plane are shown in Fig. 4. The electrical resistivity of Mg_3Bi_2 increases with temperature, showing the metallic character, and Te doping can increase the Hall carrier concentration (Supplementary Fig. 38) and reduce the electrical resistivity (Fig. 4a). The undoped Mg_3Bi_2 shows a high Seebeck coefficient of −180 μV K^{-1} at room temperature (Fig. 4b). Compared with other semimetals[27,28], which usually have an absolute Seebeck coefficient less than 100 μV K^{-1}, such a high Seebeck coefficient in Mg_3Bi_2 is quite remarkable. Slight Te doping ($x = 0.002$) can even tune the ratio of the majority carrier concentration (that is, electron concentration) to the minority carrier concentration (that is, hole concentration), thus further increasing the Seebeck coefficient (Supplementary Fig. 39). Owing to the occurrence of bipolar conduction, the Seebeck coefficient of $Mg_3Bi_{2-x}Te_x$ decreases with the increase in temperature. Mg_3Bi_2 achieves a room-temperature power factor of about 34 μW cm^{-1} K^{-2}, and it is as high as about 55 μW cm^{-1} K^{-2} for $Mg_3Bi_{1.998}Te_{0.002}$ (Fig. 4c). The thermal conductivity of $Mg_3Bi_{2-x}Te_x$ increases with temperature owing to the bipolar effect. Eventually, Mg_3Bi_2 shows a room-temperature figure of merit (zT) of about 0.35, and it is about 0.65 for $Mg_3Bi_{1.998}Te_{0.002}$. The repeatability of the electrical transport properties of $Mg_3Bi_{1.998}Te_{0.002}$ was verified (Supplementary Fig. 40). For practical application, the chemical and thermal stabilities of the material are of great importance[29–31]. The thermoelectric properties of Mg_3Bi_2 were cycled between 300 K and 573 K ten times, and the results were nearly identical (Supplementary Fig. 41). In addition, Mg_3Bi_2 was stored in dry air for 30 days and the thermoelectric properties remained highly comparable (Supplementary Fig. 42), indicating good chemical stability of the material once the isolation of the water can be guaranteed[30,31].

A comparison of the maximum tensile strain, zT and power factor among different thermoelectric materials is shown in Fig. 4f. As can be seen, $Bi_2Te_{2.7}Se_{0.3}$ and $Bi_{0.5}Sb_{1.5}Te_3$ can realize high zT and large power factor at room temperature, but their tensile strain is only less than 3%. The ductile semiconductors Ag_2S and InSe can realize a relatively higher tensile strain, but their thermoelectric performance is poor[6,8]. Most thermoelectric materials fail when a tensile strain is less than 10%. In contrast, Mg_3Bi_2 and $Mg_3Bi_{1.998}Te_{0.002}$ can realize very large tensile strain above 90% (Supplementary Fig. 43) and a high zT and power factor at room temperature. The Te doping has a negligible effect on the stress–strain behaviour and the formation of slip bands of single-crystalline Mg_3Bi_2 (Supplementary Figs. 44–47), and can be ascribed to the low doping concentration (only about 0.1 at%). As Sb alloying on Mg_3Bi_2 can effectively improve the thermoelectric properties[24,25,32], its effect on plasticity was also studied. The maximum tensile strain of $Mg_3Bi_{2-y}Sb_y$ is noticeably lower than that of the pristine Mg_3Bi_2 (Supplementary Fig. 48).

In addition, the p-type single-crystalline Mg_3Bi_2 was prepared by tuning the stoichiometry, and it also showed a large tensile strain of about 110% (Supplementary Fig. 49). Different from the electrical transport properties of Mg_3Bi_2-based materials that are dependent on the Mg content[32,33], the formation of slip bands in Mg_3Bi_2 is insensitive to the Mg stoichiometry (Supplementary Fig. 50). Owing to the anisotropy in the valence band (Supplementary Fig. 51), there are disparities in the thermoelectric transport properties of p-type Mg_3Bi_2 between the *ab* plane and the *c* plane (Supplementary Figs. 52 and 53). The room-temperature zT of the p-type single-crystalline Mg_3Bi_2 is only about 0.1, which is inferior to the n-type counterpart. Such a great difference in the thermoelectric performance between the n-type and p-type Mg_3Bi_2 can be attributed to the disparity in the valley degeneracy, which is six for the conduction band and only one for the valence band (Supplementary Fig. 54).

Conclusion

In summary, we discovered that single-crystalline Mg_3Bi_2 shows a room-temperature tensile strain of 100%. The existence of the slip bands and a high density of edge dislocations in the deformed Mg_3Bi_2 have been identified, confirming the gliding of dislocations as the underlying mechanism for plastic deformability. The calculation reveals the existence of several atomic planes with low slipping barrier energy, suggesting that multiple slip systems can be activated in Mg_3Bi_2. Dynamic bonding of Mg–Bi persists during the slipping process, thus preventing the cleavage of the atomic plane. In addition, the single-crystalline Mg_3Bi_2-based materials show a power factor of about 55 $\mu W\ cm^{-1}\ K^{-2}$ and a zT of ~0.65 at room temperature, which outperforms the state-of-the-art ductile thermoelectrics.

Online content

Any methods, additional references, Nature Portfolio reporting summaries, source data, extended data, supplementary information, acknowledgements, peer review information; details of author contributions and competing interests; and statements of data and code availability are available at https://doi.org/10.1038/s41586-024-07621-8.

1. Gelbstein, Y. et al. Physical, mechanical, and structural properties of highly efficient nanostructured n- and p-silicides for practical thermoelectric applications. *J. Electron. Mater.* **43**, 1703–1711 (2014).
2. Gahlawat, S., White, K., Ren, Z., Kogo, Y. & Iida, T. in *Advanced Thermoelectrics, Materials, Contacts, Devices, and Systems* (eds Zhifeng, R. et al.) 555–602 (CRC Press, 2017).
3. Yang, Q. et al. Flexible thermoelectrics based on ductile semiconductors. *Science* **377**, 854–858 (2022).
4. Hu, H., Wang, Y., Fu, C., Zhao, X. & Zhu, T. Achieving metal-like malleability and ductility in $Ag_2Te_{1-x}S_x$ inorganic thermoelectric semiconductors with high mobility. *The Innovation* **3**, 100341 (2022).
5. Peter, Y. & Cardona, M. *Fundamentals of Semiconductors: Physics and Materials Properties* (Springer Science & Business Media, 2010).
6. Shi, X. et al. Room-temperature ductile inorganic semiconductor. *Nat. Mater.* **17**, 421–426 (2018).
7. Oshima, Y., Nakamura, A. & Matsunaga, K. Extraordinary plasticity of an inorganic semiconductor in darkness. *Science* **360**, 772–774 (2018).
8. Wei, T.-R. et al. Exceptional plasticity in the bulk single-crystalline van der Waals semiconductor InSe. *Science* **369**, 542–545 (2020).
9. Gao, Z. et al. High-throughput screening of 2D van der Waals crystals with plastic deformability. *Nat. Commun.* **13**, 7491 (2022).
10. Hong, S. et al. Wearable thermoelectrics for personalized thermoregulation. *Sci. Adv.* **5**, eaaw0536 (2019).
11. Mao, J., Chen, G. & Ren, Z. Thermoelectric cooling materials. *Nat. Mater.* **20**, 454–461 (2021).
12. Shi, J., Guo, Z. & Sui, M. Slip system determination of dislocations in a-Ti during in situ TEM tensile deformation. *Acta Metall. Sin.* **52**, 71–77 (2016).
13. Partridge, P. The crystallography and deformation modes of hexagonal close-packed metals. *Metall. Rev.* **12**, 169–194 (1967).
14. Chin, G. Y. & Mammel, W. L. Competition among basal, prism, and pyramidal slip modes in hcp metals. *Metall. Trans.* **1**, 357–361 (1970).
15. Yoo, M. H. Slip twinning, and fracture in hexagonal close-packed metals. *Metall. Mater. Trans.* **12**, 409–418 (1981).
16. Li, G. et al. Ductile deformation mechanism in semiconductor Ag_2S. *npj Comput. Mater.* **4**, 44 (2018).
17. Ando, S. & Tonda, H. Non-basal slips in magnesium and magnesium-lithium alloy single crystals. *Mater. Sci. Forum* **350–351**, 43–48 (2000).
18. Agnew, S., Yoo, M. & Tome, C. Application of texture simulation to understanding mechanical behavior of Mg and solid solution alloys containing Li or Y. *Acta Mater.* **49**, 4277–4289 (2001).
19. Chino, Y., Kado, M. & Mabuchi, M. Compressive deformation behavior at room temperature-773 K in Mg-0.2 mass% (0.035 at.%) Ce alloy. *Acta Mater.* **56**, 387–394 (2008).
20. Al-Samman, T. & Li, X. Sheet texture modification in magnesium-based alloys by selective rare earth alloying. *Mater. Sci. Eng. A* **528**, 3809–3822 (2011).
21. Sandlöbes, S. et al. Ductility improvement of Mg alloys by solid solution: ab initio modeling, synthesis and mechanical properties. *Acta Mater.* **70**, 92–104 (2014).
22. *Atomic Reference Data for Electronic Structure Calculations, Atomic Total Energies and Eigenvalues* (NIST, 2015); https://www.nist.gov/pml/atomic-reference-data-electronic-structure-calculations/atomic-reference-data-electronic-7.
23. Schäfer, H., Eisenmann, B. & Müller, W. Zintl phases: transitions between metallic and ionic bonding. *Angew. Chem. Int. Ed.* **12**, 694–712 (1973).
24. Zhang, J. et al. Discovery of high-performance low-cost n-type Mg_3Sb_2-based thermoelectric materials with multi-valley conduction bands. *Nat. Commun.* **8**, 13901 (2017).
25. Mao, J. et al. High thermoelectric cooling performance of n-type Mg_3Bi_2-based materials. *Science* **365**, 495–498 (2019).
26. Goto, Y. et al. Band anisotropy generates axis-dependent conduction polarity of Mg_3Sb_2 and Mg_3Bi_2. *Chem. Mater.* **36**, 2018–2026 (2024).
27. Loebner, E. E. Thermoelectric power of carbons and graphite. *Phys. Rev.* **84**, 153–153 (1951).
28. Saunders, G. A., Miziumski, C., Cooper, G. S. & Lawson, A. The Seebeck coefficients of antimony and arsenic single crystals. *J. Phys. Chem. Solids* **26**, 1299–1303 (1965).
29. Shang, H. et al. N-type $Mg_3Sb_{2-x}Bi_x$ with improved thermal stability for thermoelectric power generation. *Acta Mater.* **201**, 572–579 (2020).
30. Li, A. et al. Chemical stability and degradation mechanism of $Mg_3Sb_{2-x}Bi_x$ thermoelectrics towards room-temperature applications. *Acta Mater.* **239**, 118301 (2022).
31. Wu, X. et al. Revealing the chemical instability of $Mg_3Sb_{2-x}Bi_x$-based thermoelectric materials. *ACS Appl. Mater. Interfaces* **15**, 50216–50224 (2023).
32. Tamaki, H., Sato, H. K. & Kanno, T. Isotropic conduction network and defect chemistry in Mg_3Sb_2-based layered Zintl compounds with high thermoelectric performance. *Adv. Mater.* **28**, 10182–10187 (2016).
33. Ohno, S. et al. Phase boundary mapping to obtain n-type Mg_3Sb_2-based thermoelectrics. *Joule* **2**, 141–154 (2018).

Methods

Crystal growth and material preparation

Single-crystalline samples. Mg_3Bi_2 single crystals were prepared by using the slow-cooling method. To prepare the n-type single-crystalline Mg_3Bi_2-based materials, magnesium (Mg ingots, ZNXC, 99.995%), bismuth (Bi shots, ZNXC, 99.999%) and tellurium (Te ingots, ZNXC, 99.999%) were weighed according to the nominal composition of $Mg_{3+\delta}Bi_2$ (δ = 0.05, 0.08 and 0.2), $Mg_{3.2}Bi_{2-x}Te_x$ (x = 0, 0.002 and 0.004) and $Mg_{3.2}Bi_{1.998-y}Sb_yTe_{0.002}$ (y = 0.05 and 0.10). To prepare the p-type single-crystalline Mg_3Bi_2, the nominal composition of $Mg_{2.99}Bi_2$ was used. The elements were sealed in a niobium tube (with an inner diameter of 22 mm and a length of 100 mm) with the partial pressure of argon by using an arc welder. The niobium tubes were then sealed in the quartz tube in a vacuum. The sample was heated to 1,223 K within 12 h and maintained at this temperature for 48 h, then slowly cooled to 923 K at the rate of 3 K h^{-1}, and followed by the furnace cooling.

Polycrystalline samples. Magnesium (Mg turnings, ZNXC, 99.95%), bismuth (Bi shots, ZNXC, 99.999%) and tellurium (Te ingots, ZNXC, 99.999%) were weighed according to the nominal composition of $Mg_{2.99}Bi_2$, $Mg_{3.2}Bi_2$ and $Mg_{3.2}Bi_{1.998}Te_{0.002}$. The weighed elements were loaded into a ball-milling jar in a glove box. Then the raw materials were ground into powders by a high-energy ball miller (SPEX 8000M). The mechanically alloyed powder was then loaded into a graphite die under an argon atmosphere and sintered at 973 K under uniaxial pressure of about 50 MPa for 2 min.

Composition and microstructure characterization

The phase composition and crystal structure of the cleaved Mg_3Bi_2-based single crystals were examined by X-ray diffraction with Cu K_α radiation (D/Max-2500 PC, Rigaku). The microstructure and chemical compositions of samples were investigated using a scanning electron microscope (crossbeam 350, Zeiss) equipped with energy-dispersive X-ray spectrometer. The TEM samples were prepared using focused ion beam milling. TEM and HAADF-STEM investigations were conducted using a double spherical-aberration-corrected electron microscope (JEOL ARM 200F) equipped with a cold field emission gun source operated at 200 kV.

Mechanical properties characterization

Single-crystalline (Mg_3Bi_2) and polycrystalline samples (Mg_3Bi_2, Ti, Zr, Mg, Hf, Co, $Bi_{0.5}Sb_{1.5}Te_3$, $Bi_2Te_{2.7}Se_{0.3}$, GeTe-based, PbTe-based, MgAgSb, ZrNiSn and ZrCoSb) were cut by wire electrical discharged machining and then polished with sandpaper to specified dimensions. For the compression test, the specimen of polycrystalline Mg_3Bi_2 was prepared into cylinders with a diameter of about 4 mm and a height of about 6 mm; the specimens of other materials were processed into bars with the size of $3 \times 3 \times 4$ mm^3. The specimen size was $2 \times 1 \times 12$ mm^3 for the 3-point bending test, and the test span was 7 mm and the crosshead speed was set to 0.05 mm min^{-1}. The size of the tensile specimen was shrunk based on the international standard, with the length of the narrow parallel-sided portion being about 5 mm. A universal/tensile testing machine (AGX-VD, 50 kN, Shimadzu) was used to evaluate the compressive, bending and tensile stress–strain curves of the bulk single-crystalline and polycrystalline Mg_3Bi_2 and other polycrystalline thermoelectric materials and metals. A strain rate of 0.0001 s^{-1} was applied for all the mechanical properties tests.

Thermoelectric properties characterization

The single crystals along the *ab* plane and the *c* plane were cut into the bar-shaped samples with dimensions of about 2 mm × 2 mm × 8 mm for simultaneous electrical resistivity and Seebeck coefficient measurement from 300 K to 573 K on commercial apparatuses (CTA, Cryoall and ZEM-3, Ulvac-Riko) under a helium atmosphere. The temperature-dependent Hall coefficients (R_H) were measured using the van der Pauw technique and a four-probe configuration under a reversible magnetic field of 1.5 T and an electrical current of 100 mA from 300 K to 573 K. The Hall carrier concentration (n_H) and Hall mobility (μ_H) were calculated using the relations $n_H = 1/(eR_H)$ and $\mu_H = R_H/\rho$, where e is the elementary charge. The single crystals along the *ab* plane and *c* plane were cut into the disks with dimensions of about 6 mm × 6 mm × 1 mm for the measurement of thermal diffusivity (LFA 457, Netzsch). The specific heat of the sample was measured via the heat capacity option in a physical properties measurement system (PPMS DynaCool, Quantum Design), and a differential scanning calorimeter (DSC 404 F3, Netzsch), as shown in Supplementary Fig. 55. The density of the sample was measured by the Archimedean method. Eventually, the thermal conductivity was calculated from the product of thermal diffusivity, specific heat and density.

Theoretical calculation

Calculations were performed within the framework of density functional theory by using plane-wave projector-augmented-wave methods[34] as implemented in the Vienna Ab initio Simulation Package (VASP)[35,36]. We used the generalized gradient approximation formulated by Perdew, Burke and Ernzerhof[37] as the exchange-correlation functional. The 3*s* (Mg), 6*s* and 6*p* (Bi), 4*d* and 5*s* (Ag), 5*s* and 5*p* (In), 3*s* and 3*p* (S), and 4*s* and 4*p* (Se) electrons were treated explicitly as valence electrons. The kinetic energy cut-offs for the plane-wave basis set were set to 260 eV for Mg_3Bi_2, 340 eV for Ag_2S and 320 eV for InSe. The k-point meshes with a grid spacing of $2\pi \times 0.03$ $Å^{-1}$ were used for electronic Brillouin zone integration. Structural optimizations were done through total energy minimization with the residual forces on the atoms converged to below 10^{-3} eV $Å^{-1}$. To properly take into account the long-range van der Waals interactions that play a non-ignorable role in the layered Ag_2S and InSe, the SCAN+rVV10 functional[38] was adopted. The slipping barrier energies were calculated for all potential slip systems under rigid slip constraints. A series of Mg_3Bi_2 and Ag_2S supercells were utilized to calculate the slipping barrier energies, and maintain the translational periodicity of the crystal structure during the simulated sliding. The chemical bonding was extracted from the VASP wave functions by adopting the LOBSTER package[39–42].

The electronic structures of Mg_3Bi_2 were calculated by utilizing the modified Becke–Johnson potential of Tran and Blaha, known for providing an accurate electronic band structure of semiconductors[43,44]. A tuning parameter (system-dependent c parameter in the modified Becke–Johnson potential) of 1.2 was employed and the obtained overlap between valence and conduction bands was 0.05 eV, in good agreement with the experiment results. Spin–orbit coupling was included as it is potentially important for the electronic structure of heavy p-electron systems such as Mg_3Bi_2. For the self-consistent calculations, a $21 \times 21 \times 13$ k-point mesh was used to sample the Brillouin zone. The maximally localized Wannier function method was employed to generate the Fermi surface as implemented in the Wannier90 code[45–47]. The Fermi surface was visualized using the XCrySDen software[48]. The resulting electronic structures were used to obtain electrical transport properties. This was done using semiclassical Boltzmann theory[49] and the BoltzTraP2[50] code with first-principles electronic structures evaluated on approximately 570,000 k-points in the irreducible Brillouin zone.

Data availability

The data supporting the findings of this study are available within the paper or from the corresponding authors. Source data are provided with this paper.

34. Blöchl, P. E. Projector augmented-wave method. *Phys. Rev. B* **50**, 17953 (1994).
35. Kresse, G. & Furthmüller, J. Efficient iterative schemes for ab initio total-energy calculations using a plane-wave basis set. *Phys. Rev. B* **54**, 11169 (1996).
36. Kresse, G. & Furthmüller, J. Efficiency of ab-initio total energy calculations for metals and semiconductors using a plane-wave basis set. *Comput. Mater. Sci.* **6**, 15–50 (1996).
37. Perdew, J. P., Burke, K. & Ernzerhof, M. Generalized gradient approximation made simple. *Phys. Rev. Lett.* **77**, 3865 (1996).
38. Peng, H., Yang, Z.-H., Perdew, J. P. & Sun, J. Versatile van der Waals density functional based on a meta-generalized gradient approximation. *Phys. Rev. X* **6**, 041005 (2016).
39. Dronskowski, R. & Blöchl, P. E. Crystal orbital Hamilton populations (COHP): energy-resolved visualization of chemical bonding in solids based on density-functional calculations. *J. Phys. Chem.* **97**, 8617–8624 (1993).
40. Deringer, V. L., Tchougréeff, A. L. & Dronskowski, R. Crystal orbital Hamilton population (COHP) analysis as projected from plane-wave basis sets. *J. Phys. Chem. A* **115**, 5461–5466 (2011).
41. Maintz, S., Deringer, V. L., Tchougréeff, A. L. & Dronskowski, R. Analytic projection from plane-wave and PAW wavefunctions and application to chemical-bonding analysis in solids. *J. Comput. Chem.* **34**, 2557–2567 (2013).
42. Maintz, S., Deringer, V. L., Tchougréeff, A. L. & Dronskowski, R. LOBSTER: a tool to extract chemical bonding from plane-wave based DFT. *J. Comput. Chem.* **37**, 1030–1035 (2016).
43. Tran, F. & Blaha, P. Accurate band gaps of semiconductors and insulators with a semilocal exchange-correlation potential. *Phys. Rev. Lett.* **102**, 226401 (2009).
44. Singh, D. J. Electronic structure calculations with the Tran–Blaha modified Becke–Johnson density functional. *Phys. Rev. B* **82**, 205102 (2010).
45. Yates, J. R., Wang, X., Vanderbilt, D. & Souza, I. Spectral and Fermi surface properties from Wannier interpolation. *Phys. Rev. B* **75**, 195121 (2007).
46. Mostofi, A. A. et al. Wannier90: a tool for obtaining maximally-localised Wannier functions. *Comput. Phys. Commun.* **178**, 685–699 (2008).
47. Mostofi, A. A. et al. An updated version of Wannier90: a tool for obtaining maximally-localised Wannier functions. *Comput. Phys. Commun.* **185**, 2309–2310 (2014).
48. Kokalj, A. XCrySDen—a new program for displaying crystalline structures and electron densities. *J. Mol. Graph. Model.* **17**, 176–179 (1999).
49. Jin, Y. et al. High-throughput deformation potential and electrical transport calculations. *npj Comput. Mater.* **9**, 190 (2023).
50. Madsen, G. K., Carrete, J. & Verstraete, M. J. BoltzTraP2, a program for interpolating band structures and calculating semi-classical transport coefficients. *Comput. Phys. Commun.* **231**, 140–145 (2018).

Acknowledgements This work was supported by the National Key Research and Development Program of China (2023YFB3809400), the Shenzhen Science and Technology Program (KQTD20200820113045081) and the Outstanding Young Scholar Team of the Guangdong Basic and Applied Basic Research Foundation (2024B1515040022). J.M. acknowledges the financial support from the Shenzhen Science and Technology Program (RCJC20221008092725020) and the Shenzhen Fundamental Research Projects (JCYJ20210324132808020). Q.Z. acknowledges the financial support from the National Natural Science Foundation of China (52172194) and the Shenzhen Science and Technology Program (RCJC20210609103733073). F.C. acknowledges the financial support from the Shenzhen Fundamental Research Program (JCYJ20220818102408017). Y.F. acknowledges the financial support from the National Natural Science Foundation of China (22090044). Y.W. acknowledges the financial support from the National Natural Science Foundation of China (12074409, 12374021). We thank D. Singh for the discussion on theoretical calculation; M. L. Sui for the discussion on the analysis of dislocations; Y. L. Zhao for the discussion on mechanical properties; and H. Gao and B. Q. Luo for their help in mechanical properties characterization.

Author contributions J.M., Q.Z. and P.Z. conceived the idea. P.Z., X.M. and J.Q. prepared the single crystals and the polycrystalline Mg_3Bi_2-based materials. Y.Z. and W.X. prepared the TEM samples. Y.W., Y.Z. and W.X. performed the TEM characterization and analysed the data. P.Z., J.Q., J.C. and X.W. characterized and analysed the thermoelectric properties. P.Z. and S.Y. characterized the low-temperature specific heat. P.Z., T.Z., S.H., G.X., X.L. and L.Z. characterized and analysed the mechanical properties. Y.F. and H.M. performed the first-principles calculations. J.M., Y.F., P.Z., S.Z. and F.C. analysed the data. J.M., Q.Z., Y.F. and P.Z. wrote and edited the paper. All authors contributed helpful discussion to this work.

Competing interests The authors declare no competing interests.

Additional information

Supplementary information The online version contains supplementary material available at https://doi.org/10.1038/s41586-024-07621-8.

Correspondence and requests for materials should be addressed to Jun Mao, Yuhao Fu, Yumei Wang or Qian Zhang.

Peer review information *Nature* thanks Takao Mori, Bed Poudel and the other, anonymous, reviewer(s) for their contribution to the peer review of this work. Peer reviewer reports are available.